ACS OMEGA

Open Access

http://pubs.acs.org/journal/acsodf

Article

Crystal Structure Modification and Dielectric Properties of Sr- and La-Containing $A_2B_2O_7$ Thin Films for High-Temperature Operational Film Capacitors

Takahiro Nagata,* Toyohiro Chikyow, and Akira Ando

Cite This: *ACS Omega* 2024, 9, 25968−25975

Read Online

ACCESS | Metrics & More | Article Recommendations | Supporting Information

ABSTRACT: In order to obtain thermally stable thin-film materials with high dielectric constant, $A_2B_2O_7$ thin films ($Sr_2Ta_2O_7$, $Sr_2Nb_2O_7$, $La_2Zr_2O_7$, and $La_2Ti_2O_7$) containing Sr or La and their solid solutions were grown on Pt/Ti/SiO_2/Si substrates by RF sputtering and their crystal structures and dielectric properties were investigated. The $Sr_2Ta_2O_7$ and $La_2Ti_2O_7$ films exhibit highly oriented crystal structures. By contrast, the $Sr_2Nb_2O_7$ and $La_2Zr_2O_7$ films exhibit polycrystalline structures. The leakage properties of the Sr-containing films are lower and more stable in the high-temperature region (up to 300 °C) than those of the La-containing films. Among the investigated films, the $Sr_2Ta_2O_7$ film grown at 500 °C and annealed at 900 °C shows the most stable dielectric constant with respect to temperature in the temperature range from room temperature to 300 °C. In addition, the $xSr_2Ta_2O_7-(1-x)La_2Ti_2O_7$ solid solutions exhibit enhanced dielectric properties at $x = 0.35$. The dielectric constant is greater than 100, and its variation with temperature is less than 10%. The Sr-containing $A_2B_2O_7$ ferroelectric thin films have potential applications as high-temperature film capacitors that can operate at temperatures as high as 300 °C.

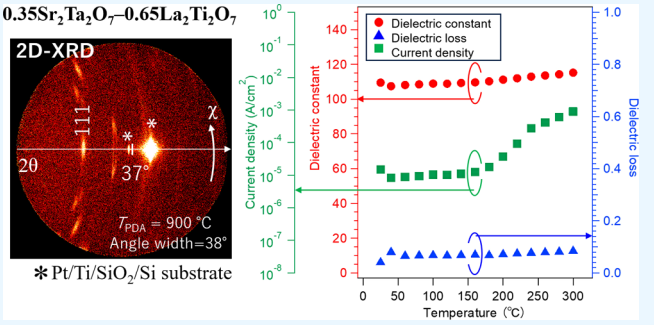

1. INTRODUCTION

The demand for high-switching-frequency power semiconductor devices for compact and efficient energy-saving applications in the home and automobile, as well as in the aerospace, geothermal exploration, and power transmission fields has been increasing. Many of these applications involve high temperatures and harsh environments, so various high-power active devices based on wide-bandgap semiconductors such as SiC, GaN, and diamond have been developed.[1−4] In particular, SiC-based devices have advanced to the commercial manufacturing stage, and SiC-based transistors and Schottky diodes that can operate at temperatures above 250 °C have been developed.[5,6] For these applications, high-temperature operational passive devices should be urgently developed to advance the module and system levels.[7] In the case of capacitors, currently available capacitors can only operate efficiently at temperatures of 175 °C or lower. Therefore, a thin-film capacitor that can operate at high temperatures and can be monolithically integrated close to the active device should be developed. For this application, we have previously investigated Bi-containing $BaTiO_3$-based relaxor ferroelectrics that exhibit high dielectric constants and are free of hazardous elements such as Pb.[8−10] We have demonstrated the epitaxial thin-film growth of a $BaTiO_3-Bi(Mg_{2/3}Nb_{1/3})O_3$ relaxor ferroelectric thin film on a $SrTiO_3$ substrate.[11] Although the $BaTiO_3-Bi(Mg_{2/3}Nb_{1/3})O_3$ epitaxial thin films exhibited a high dielectric constant,[12,13] their dielectric constant increased sharply at ∼100 °C, which is related to the Curie−Weiss temperature of $BaTiO_3$. Their dielectric properties were found to be degraded by the out-diffusion of Bi in the film in the high-temperature region. In terms of high-temperature stability of dielectric constant from room temperature to 300 °C, $K_{0.5}Na_{0.5}NbO_3$ related materials have been reported in bulk,[14,15] but there is a problem of composition controllability in thin-film synthesis in K-, Na-, and Bi-containing systems in solid-solution formation. In contrast, as a material that does not contain Bi and has a Curie temperature in the high-temperature range, ferroelectrics having a layered perovskite structure with alternating layers of perovskite units and other layers in the long-axis direction of the crystal are other candidates. Ferroelectric materials with the layered perovskite structure, such as $Sr_2Nb_2O_7$ and $Sr_2Ta_2O_7$, which have also been studied as photocatalytic materials,[16,17] show a high dielectric constant greater than 100 at both high and low temperatures.[18−20] However, because of the crystallographic direction dependence of the Curie−Weiss

Received: January 24, 2024
Revised: May 18, 2024
Accepted: May 22, 2024
Published: June 7, 2024

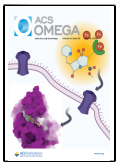

Table 1. Physical Properties of $Sr_2Ta_2O_7$, $Sr_2Nb_2O_7$, $La_2Zr_2O_7$, and $La_2Ti_2O_7$

material ($A_2B_2O_7$)	lattice structure	symmetry group	lattice constant (Å)			valence number[a]		ionic radius (Å)[a]	
			a =	b =	c =	A-site	B-site	A-site	B-site
$Sr_2Ta_2O_7$	base-centered orthorhombic	$Cmcm$ (63)	3.937	27.198	5.692	2+	5+	1.18	0.64
$Sr_2Nb_2O_7$	base-centered orthorhombic	$Cmc2_1$ (36)	3.957	26.787	5.701	2+	5+	1.18	0.64
$La_2Zr_2O_7$	face-centered cubic	$F23$ (196)	10.804			3+	4+	1.032	0.72
$La_2Ti_2O_7$	monoclinic	$P2_1/^a$ (11)	13.015	5.545	7.817	3+	4+	1.032	0.605

[a]6-coordinate.

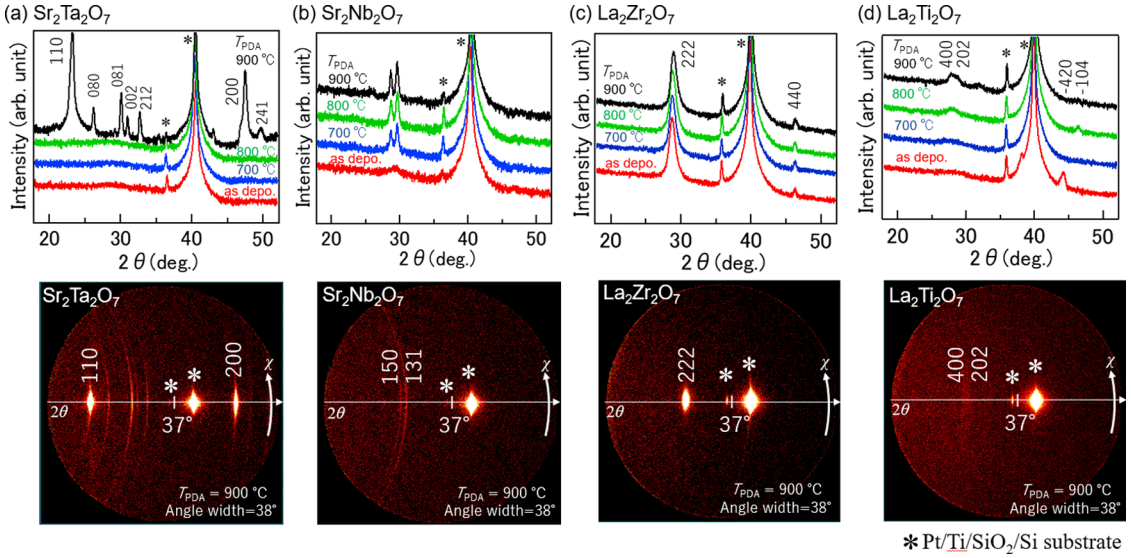

Figure 1. XRD $2\theta-\omega$ plots for as-deposited films and films annealed at 700, 800, and 900 °C (top) and 2D-XRD images (bottom) of (a) $Sr_2Ta_2O_7$, (b) $Sr_2Nb_2O_7$, (c) $La_2Zr_2O_7$, and (d) $La_2Ti_2O_7$ films annealed at 900 °C.

temperature, the temperature stabilities of the dielectric constant from room temperature to 300 °C for these thin films are unknown.

In the present study, we investigated A- and B-site substitutions in Sr- and La-containing $A_2B_2O_7$ materials as single phases and as solid solutions prepared by radiofrequency (RF) sputtering in order to understand and improve their dielectric properties and thermal stability. First, crystallized thin films of $A_2B_2O_7$ materials were prepared and their basic physical properties were evaluated. Next, compositionally graded solid-solution films were prepared using a combinatorial method,[21,22] and their physical properties were also systematically studied. For the synthesis of solid-solution thin films, $A_2B_2O_7$ ferroelectrics containing Sr or La (i.e., $Sr_2Ta_2O_7$,[19] $Sr_2Nb_2O_7$,[19] $La_2Zr_2O_7$,[23] and $La_2Ti_2O_7$[24]) were selected for substitution at the A and/or B sites on the basis of their valence numbers and ionic radii (Table 1). We also improved the physical properties of the compositions expected to exhibit higher dielectric constants and enhanced temperature stability of their dielectric constants; we found that the Sr-based $A_2B_2O_7$ solid-solution film exhibited a substantially improved dielectric constant and enhanced stability of its dielectric constant in the temperature range from room temperature to 300 °C.

2. EXPERIMENTAL SECTION

The substrate was Si(100) with a 300-nm-thick SiO_2 layer formed by thermal oxidation. As the bottom electrode, a 100-nm-thick (111)-oriented Pt/10-nm-thick Ti layer was deposited on the substrate by DC sputtering, followed by RF sputtering of an $A_2B_2O_7$ thin film. For RF sputtering, $Sr_2Ta_2O_7$, $Sr_2Nb_2O_7$, $La_2Zr_2O_7$, and $La_2Ti_2O_7$ ceramic targets (Toshima Manufacturing, metallic purity <99.9%) were used. The substrate temperature was set in the range 350−600 °C. The base pressure in the vacuum chamber was less than 1×10^{-5} Pa, the pressure of the sputtering gas was 1 Pa, and the flow rate of the sputtering gas was 5% O_2 to Ar-based mixed gas. The RF power and the film thickness were at 50 W and 100 nm, respectively. Combinatorial methods were used to prepare compositionally graded solid-solution films. Details are available elsewhere.[21,22] Postdeposition annealing (PDA) was performed by rapid thermal annealing (Advance Riko, MILA-3000) at 700, 800, and 900 °C for 5 min under an O_2 (purity: 6N) flow rate of 0.2 L/min and a temperature rise time of 2 min; the samples were allowed to cool naturally in the furnace.

The crystal structures of the thin films were analyzed by two-dimensional X-ray diffraction (2D-XRD) using an instrument equipped with a 5 kW rotating Cu anode and a large-area 2D detector [Bruker AXS D8 Discover Super Speed with a general area detector diffraction system (GADDS)]. 2D-XRD can simultaneously detect 2θ and χ angles from a part of the Debye−Scherrer ring. In the 2D-XRD image, a spot pattern indicates a single-crystalline or highly oriented structure. By contrast, a ring pattern indicates a polycrystalline structure. In the present study, a conventional $2\theta-\omega$ plot is an integrated pattern of the 2D-XRD image along the ω direction with an angle width of 20°. The peak position was calibrated on the basis of the (400) reflection (2θ = 69.1°[25]) from the Si substrate. The surface morphology was observed by atomic force microscopy (AFM, Hitachi High-Technologies,

https://doi.org/10.1021/acsomega.4c00788
ACS Omega 2024, 9, 25968−25975

AFM5000II) under atmospheric conditions. For electrical measurements, a 150-nm-thick Pt top electrode with a diameter of 110 μm was deposited by DC sputtering using a metal stencil mask. The electrical properties were evaluated at atmospheric pressure and in the dark via current density−voltage ($J-V$), capacitance−voltage ($C-V$), and capacitance−frequency ($C-f$) measurements using a semiconductor parametric analyzer (Keysight Technologies, B1500A). The bottom electrode was biased, and the top electrode was grounded. For the $J-V$ measurements, the compliance current was set to 1 mA. The temperature dependence of the electrical properties was evaluated under vacuum conditions at a pressure of less than 10^{-2} Pa and in the temperature range from room temperature to 300 °C.

3. RESULTS AND DISCUSSION

3.1. Single-Phase Films. *3.1.1. Crystallization Conditions.* Figure 1a,b shows XRD $2\theta-\omega$ plots of deposited $Sr_2Ta_2O_7$ and $Sr_2Nb_2O_7$ films annealed at 700, 800, and 900 °C. $Sr_2Ta_2O_7$ crystallized at 900 °C. This is 100 °C higher than the crystallization temperature of the powder sample reported by Okuwada;[26] however, the film grown on the $Pt/SiO_2/Si$ substrate by sol−gel method also reported an increase in crystallization temperature, which may be an effect of the substrate. As shown in Figure 1a, the 2D-XRD image of the $Sr_2Ta_2O_7$ film shows two spot patterns and several small ring patterns at 2θ values of 22.7 and 46.9°, corresponding to the (110) and (200) reflections, respectively, for an orthorhombic crystal structure.[27] For the (110) reflection, in particular, the orientation was estimated to be 0.81 on the basis of the Lotgering factor.[28] The other reflections contained contributions mainly in the [001] direction. These results indicate that the thin films preferred the (110)-oriented structure. By contrast, crystallization of $Sr_2Nb_2O_7$ was observed at 700 °C. The 2D-XRD image of $Sr_2Nb_2O_7$ shows ring patterns at 2θ angles of 28.1 and 29.1°, corresponding to the (151) and (131) reflections for an orthorhombic crystal structure[29] and indicating that the sample is polycrystalline. This crystallization temperature is consistent with that reported for a $Sr_2Nb_2O_7$ film on the $Pt/SiO_2/Si$ substrate grown by the sol−gel method, which showed a (010) crystal orientation.[30]

Figure 1c,d shows XRD patterns for $La_2Zr_2O_7$ and $La_2Ti_2O_7$ films annealed at 700, 800, and 900 °C after deposition. The patterns for the $La_2Zr_2O_7$ film show a (111) reflection at 28.8°, and the face-centered cubic structure[31] was confirmed in all of the films. In the 2D-XRD pattern in Figure 1c, spot peaks are observed, indicating that the $La_2Zr_2O_7$ film was grown epitaxially on the (111)-oriented Pt film.[32] The crystallization temperature and oriented structure are similar to those described in previous reports.[23,32] For the $La_2Ti_2O_7$, the crystallization temperature is higher than that of other films. Even for the film annealed at 900 °C, the 2D-XRD pattern shows a weak pattern [Figure 1d]. The reflections at 27.7 and 28.5° correspond to the (400) and (202) planes of the monoclinic crystal structure.[33] To obtain a crystallized $La_2Ti_2O_7$ film, high-temperature annealing is required, which is consistent with a previous report by Shao et al.,[34] who obtained a crystallized $La_2Ti_2O_7$ film on a (110) $SrTiO_3$ substrate after annealing a sol−gel deposited $La_2Ti_2O_7$ film at 950 °C and subsequently confirmed its ferroelectric properties. The high orientation is also attributed to the lattice matching with the Pt substrate. Under the present condition, the face-centered cubic structure of $La_2Zr_2O_7$ is the same as that of Pt, and the lattice matching with the 3-fold period of Pt by matching with the (111) plane of $La_2Zr_2O_7$ may also be responsible for the high orientation.

Table 2 summarizes the crystallization properties as a function of growth and postannealing temperatures. On the basis of the 2D-XRD images (Figure 1), we classified the crystallinity into four phases: an amorphous phase (AM), a weak polycrystalline phase (PW), an oriented polycrystalline phase (PC), and a highly oriented polycrystalline phase (OC). When the annealing temperature was 900 °C and the deposition temperature was greater than 500 °C, all of the films exhibited the aforementioned highly oriented structure. Detailed physical properties of the films deposited at 500 °C were investigated.

Table 2. Relationship of the Crystallinity of Target Materials to the Film Growth Temperature (T_{sub}) and the PDA Temperature (T_{PDA})

$T_{sub.}$ \ T_{PDA}	As depo.	700 °C	800 °C	900 °C
350 °C	(a) AM (b) PW (c) AM (d) OC	(a) AM (b) PC (c) AM (d) OC	(a) AM (b) PC (c) AM (d) OC	(a) AM (b) PC (c) AM (d) OC
400 °C	(a) AM (b) PW (c) AM (d) OC	(a) AM (b) PC (c) AM (d) OC	(a) AM (b) PC (c) AM (d) OC	(a) PC (b) PC (c) PW (d) OC
450 °C	(a) AM (b) PW (c) AM (d) OC	(a) AM (b) PC (c) AM (d) OC	(a) AM (b) PC (c) PW (d) OC	(a) PC (b) PC (c) PW (d) OC
500 °C	(a) AM (b) PW (c) AM (d) OC	(a) AM (b) PC (c) AM (d) OC	(a) AM (b) PC (c) PW (d) OC	(a) PC (b) PC (c) PC (d) OC
550 °C	(a) AM (b) PW (c) AM (d) OC	(a) AM (b) PC (c) AM (d) OC	(a) AM (b) PC (c) PW (d) OC	(a) PC (b) PC (c) PC (d) OC
600 °C	(a) AM (b)− (c) PW (d) OC	(a) AM (b)− (c) AM (d) OC	(a) AM (b)− (c) PC (d)OC	(a) PC (b)− (c) PC (d) OC

Materials: (a) $Sr_2Ta_2O_7$, (b) $Sr_2Nb_2O_7$, (c) $La_2Ti_2O_7$, (d) $La_2Zr_2O_7$

Crystallinity : AM: amorphous, PW: polycrystalline (weak)
PC: polycrystalline (strong/oriented),
OC: highly oriented crystal

3.1.2. Physical Properties of Single-Phase Films. Figure 2 shows AFM images of the as-deposited films and the films annealed at 900 °C. The La-containing films are composed of grains with a diameter of a few tens of nanometers. By contrast, the Sr-containing films contain larger grains than the La-containing films. Except for the $Sr_2Nb_2O_7$ film, the surface structure and roughness of the annealed films were similar to those of the as-deposited films. The $Sr_2Nb_2O_7$ film showed an increase in grain growth and surface roughness, which was confirmed by the increase in the root-mean-square (RMS) value of the grain size from 2.70 to 6.6 nm after annealing the film at 900 °C. The RMS values for the other films were less than 1.6 nm.

Figure 3 shows the room-temperature electrical properties of the as-deposited films and the films annealed at 700, 800, and 900 °C. For $Sr_2Ta_2O_7$, the film annealed at 900 °C, which exhibited a crystalline structure, showed a decrease in leakage current and stable dielectric behavior [Figure 3a-i,ii]. At the measurement frequency of 1 MHz, the dielectric constant of the $Sr_2Ta_2O_7$ film annealed at 900 °C was 53. For the $Sr_2Nb_2O_7$ films, those annealed at 800 and 900 °C, which exhibited a grain structure, showed an increase in leakage current. AFM results show significant grain growth in the $Sr_2Nb_2O_7$ film annealed at 900 °C, and the leakage current of the film annealed at high temperature could be improved by grain size and grain boundary control. The $Sr_2Nb_2O_7$ film

https://doi.org/10.1021/acsomega.4c00788
ACS Omega 2024, 9, 25968−25975

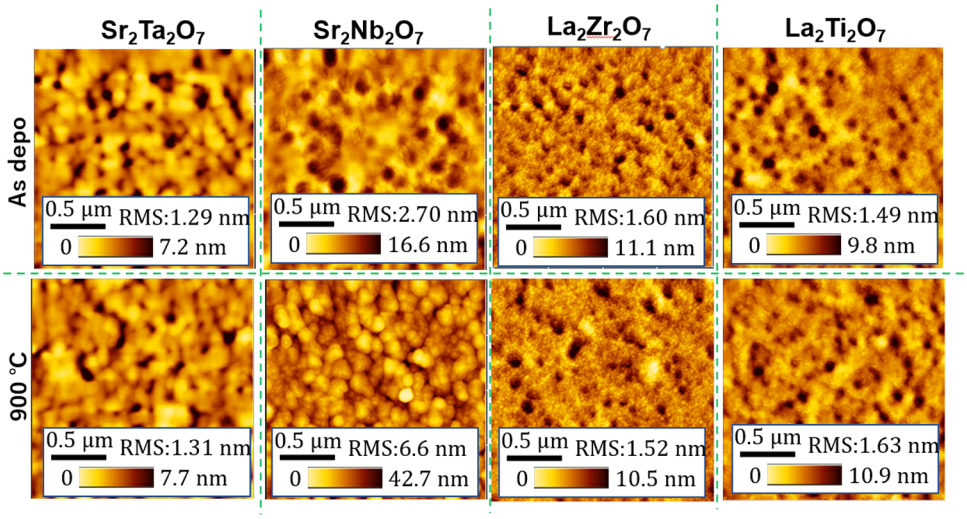

Figure 2. AFM images of $Sr_2Ta_2O_7$, $Sr_2Nb_2O_7$, $La_2Zr_2O_7$, and $La_2Ti_2O_7$ films. The top images are as-deposited films. The bottom images are films annealed at 900 °C.

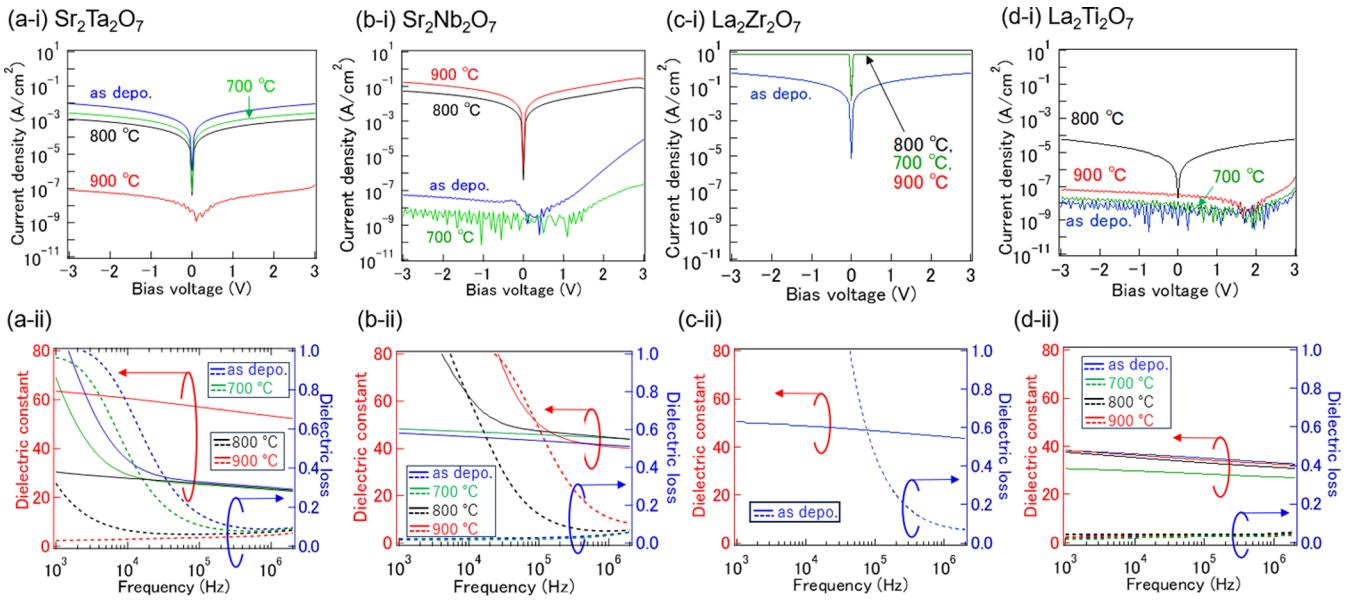

Figure 3. (i) $J-V$ and (ii) $C-f$ properties of as-deposited and annealed films of (a) $Sr_2Ta_2O_7$, (b) $Sr_2Nb_2O_7$, (c) $La_2Zr_2O_7$, and (d) $La_2Ti_2O_7$ at room temperature under atmospheric conditions. Dielectric constants for samples with dielectric loss greater than 1 are shown as reference data.

annealed at 700 °C, which was crystalline and exhibited a dielectric constant of 45 at 1 MHz, showed a lower leakage current and a higher dielectric constant than the other $Sr_2Nb_2O_7$ films. The $La_2Zr_2O_7$ films with highly oriented structures showed a high dielectric loss because of their poor leakage characteristics [Figure 3c-i]. By contrast, the $La_2Ti_2O_7$ films with a predominantly amorphous structure exhibited more stable dielectric properties than the other films, with a dielectric constant of ∼40 [Figure 3d-ii]. Note that the $C-V$ properties at 1 MHz for all of the films showed no hysteresis response corresponding to ferroelectricity (Supporting Information, Figure S2).

Figure 4 shows the dielectric constant and dielectric loss versus sample temperature at a frequency of 1 MHz and a bias voltage of +3 V for the $Sr_2Ta_2O_7$ film annealed at 900 °C, the $Sr_2Nb_2O_7$ film annealed at 700 °C, and the La_2TiO_7 film annealed at 900 °C. The temperature stability of dielectric constant ($\Delta C/C$) from room temperature to 300 °C is defined as $\frac{\Delta C}{C} = \frac{\varepsilon_{max} - \varepsilon_{min}}{\varepsilon_{RT}} \times 100\%$, where ε_{max}, ε_{min}, and ε_{RT} are the maximum, minimum, and room-temperature dielectric constants, respectively. The $\Delta C/C$ values for the $Sr_2Nb_2O_7$ and La_2TiO_7 films were 35.6 and 24.1%, respectively. By contrast, the $Sr_2Ta_2O_7$ film showed a $\Delta C/C$ of 4.9% and a dielectric constant of ∼50. These dielectric constants and temperature stability are similar to those for the electrical properties of the corresponding bulk single crystals. The (110) plane, which is the preferred orientation plane for the 900 °C-annealed $Sr_2Ta_2O_7$ film, is inclined 8.24° relative to the (100) plane. The reported dielectric constant for the (100) plane of a $Sr_2Ta_2O_7$ single crystal is ∼40 at 1 MHz, and the dielectric constant has been reported to be nearly constant from −50 °C to room temperature.[16] Because of the combination of the temperature dependence of the dielectric constants for $Sr_2Nb_2O_7$ and $Sr_2(Ta_{1-x}Nb_x)O_7$ solid-solution crystals,[19] the (100)-oriented $Sr_2Ta_2O_7$ film should exhibit an almost

https://doi.org/10.1021/acsomega.4c00788
ACS Omega 2024, 9, 25968−25975

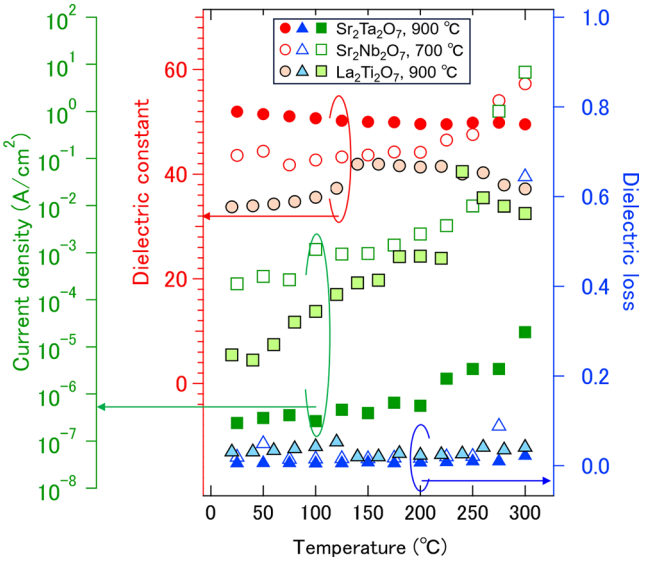

Figure 4. Temperature dependence of the dielectric constant (circles), dielectric loss (triangles), and current density (squares) of a $Sr_2Ta_2O_7$ film annealed at 900 °C, an as-deposited $Sr_2Nb_2O_7$ film annealed at 700 °C, and a $La_2Ti_2O_7$ film annealed at 900 °C.

constant dielectric constant from room temperature to 300 °C. In addition, the (001)-oriented $Sr_2Ta_2O_7$ single crystal showed a high dielectric constant of ∼600; however, a decrease of the dielectric constant near room temperature was confirmed by the Curie−Weiss temperature of −107 °C.[19] The coexistence of other planes should increase the dielectric constant.

3.2. Solid-Solution Films. *3.2.1. B-Site Replacement.* On the basis of the aforementioned results for single-phase thin films, we selected $Sr_2Ta_2O_7$ as the base material. To confirm the controllability of the crystal structure and orientation, we first attempted B-site substitution in the $Sr_2Ta_2O_7$−$Sr_2Nb_2O_7$ solid-solution system. Figure 5 shows XRD patterns for

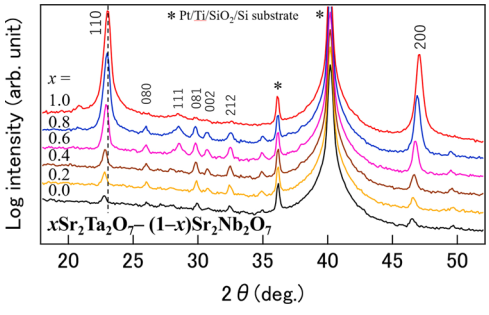

Figure 5. XRD $2\theta-\omega$ plots for $x Sr_2Ta_2O_7-(1-x)Sr_2Nb_2O_7$ solid-solution films annealed at 900 °C versus the composition change.

composition-graded solid-solution films deposited at 500 °C and annealed at 900 °C. The crystal structure of $Sr_2Ta_2O_7$ is the major structure. The (110) refraction for the $Sr_2Ta_2O_7$ structure was confirmed.

As the compositional fraction of $Sr_2Ta_2O_7$ decreased, a tail formed on the low-angle side of the (110) diffraction peak in the XRD pattern and the peak exhibited an increase in asymmetry, an increase in the full-width at half-maximum, a peak shift toward the low-angle side, and a decrease in intensity; these observations indicate that the crystallinity decreased (Supporting Information, Figure S3). For the peak shift, according to JCPDS Powder Diffraction File-2 (PDF),[27,30] the (110) of $Sr_2Nb_2O_7$ is on the 0.1° lower angle side than the (110) of $Sr_2Ta_2O_7$, so the trend is consistent with the experimental results. However, in the experiment, the angle difference between the $Sr_2Ta_2O_7$ side and the $Sr_2Nb_2O_7$ side is 0.3°, and the difference is thought to have increased due to the strain from the substrate. The unit lattice length for the (111)-oriented surface of Pt, which was the bottom electrode material on the substrate, was $\sqrt{2}a$ = 5.548 Å (Pt has a cubic structure with a = 3.923 Å[35]) and the lattice mismatch with the (110)-oriented $Sr_2Ta_2O_7$ thin film should have caused a decrease in the plane spacing and a shift of the XRD peak toward the high-angle side as a result of an increase in the out-of-plane tensile strain of the film. The results for single-phase $Sr_2Nb_2O_7$ are dominated by growth along the ⟨131⟩ direction, which has a large lattice mismatch with the (111)-oriented Pt surface. The change in orientation of the pure $Sr_2Nb_2O_7$ region from (150) and (131) to (110) is considered to be a contraction resulting from the crystallinity degradation caused by the change in stable planes and the stronger influence of the c-axis direction. In addition, in the sputtering setup, obtaining 100% single-phase films at both edges of the composition gradient region is difficult because the distance between the substrate surface and the moving mask, which controls the film thickness during the deposition, is less than 1 mm. Each edge must contain a few percent of another material. The change in electrical properties due to this heterogeneity was confirmed by the tendency of the leakage current to increase with increasing Nb content (Supporting Information, Figure S4). Even in the region where the leakage current is favorable, no results corresponding to enhanced electrical characteristics of the single phase were obtained. The intermediate region maintains a linear change in composition, as confirmed by X-ray fluorescence spectroscopy [Supporting Information, Figure S1c]. Thus, the small amount of $Sr_2Nb_2O_7$ degraded the crystallinity and grain growth of the $Sr_2Ta_2O_7$−$Sr_2Nb_2O_7$ film. Notably, the same trend is more pronounced for $La_2Zr_2O_7$−$La_2Ti_2O_7$ (Supporting Information, Figure S5), which is a cubic crystal structure and thus exhibits an orientation similar to that of the (111)-oriented Pt surface, resulting in a highly oriented film with no hetero-oriented components. By contrast, when the proportion of $La_2Ti_2O_7$ is increased, the effect of the increase in the long-axis direction of the monoclinic structure becomes more pronounced, especially because the a-axis of $La_2Ti_2O_7$ is longer than the unit lattice length $\sqrt{2}a$ = 15.279 Å of (111) $La_2Zr_2O_7$, which tends to be on the tensile strain side. Therefore, we considered that the change is more pronounced in (111) $La_2Zr_2O_7$. The results of the electrical measurements show that the increase in the proportion of $La_2Ti_2O_7$ did not improve the leakage current characteristics.

3.2.2. A- and B-Site Replacement. B-site substitution did not dramatically affect the continuous change in crystal structure. Given the relationship between the ionic radii, the crystallization temperature in Tables 1 and 2, and the fabrication conditions, we next attempted simultaneous A- and B-site substitution. In addition, given the change in the electrical properties of the single-phase thin films (Figure 3), we fabricated a solid-solution thin film of $Sr_2Ta_2O_7$ and $La_2Ti_2O_7$ [$xSr_2Ta_2O_7-(1-x)La_2Ti_2O_7$] at substrate temperatures of 500 and 550 °C and a PDA temperature of 900 °C.

Figure 6 shows the composition dependence of the XRD patterns: the $La_2Ti_2O_7$ composition side shows a crystal

https://doi.org/10.1021/acsomega.4c00788
ACS Omega 2024, 9, 25968−25975

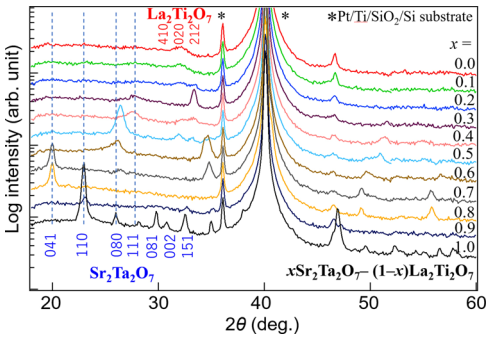

Figure 6. XRD 2θ–ω plots of $x\mathrm{Sr_2Ta_2O_7}$–$(1-x)\mathrm{La_2Ti_2O_7}$ solid-solution films annealed at 900 °C versus the composition change.

structure corresponding to $La_2Ti_2O_7$ for films with x values as large as 0.2. By contrast, the $Sr_2Ta_2O_7$ side shows diffraction peaks from several different planes of the crystal structure corresponding to $Sr_2Ta_2O_7$. Notably, the results for each composition of x = 0 and x = 1 differ from those of the corresponding single-phase materials because of the effect of the sputtered particles wrapping around the composition control mask, as previously described. With respect to the effects of crystallization, the crystal structures of $x\mathrm{Sr_2Ta_2O_7}$–$(1-x)\mathrm{La_2Ti_2O_7}$ were strongly influenced by the $Sr_2Ta_2O_7$ structure, which was more crystallized in the single phase under the present fabrication conditions, and the $Sr_2Ta_2O_7$ crystal structure was maintained up to x = 0.3.

The dependence of the dielectric constant on the orientation was also investigated. On the basis of the leakage current characteristics, the dielectric constants and orientations were characterized at temperatures of 500 and 550 °C during film formation; the dielectric constant versus composition and the respective principal orientation information are shown in Figure 7. The changes in dielectric constant correspond to three major orientations—(041), (010), and (111)—in the compositional region that exhibited effective dielectric constants. The (111)-oriented region exhibited the highest dielectric constant. Nanamatsu et al. reported the dependence of the dielectric constant on the crystal plane orientation and

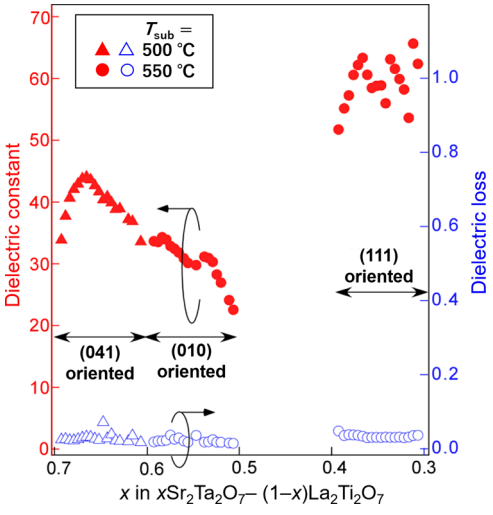

Figure 7. Dielectric constant (solid symbols) and dielectric loss (open symbols) for $x\mathrm{Sr_2Ta_2O_7}$–$(1-x)\mathrm{La_2Ti_2O_7}$ solid-solution films deposited at 500 and 550 °C and annealed at 900 °C.

temperature in a single-crystal sample of the $Sr_2Ta_2O_7$–$Sr_2Nb_2O_7$ solid-solution system.[19] The Curie temperatures of the dielectric constants of the planes perpendicular to the c-axes have composition dependence. The Curie temperature was reported to depend on the substitution of the A-site, and the substitution of the A-site with an element of smaller ionic radius increases the Curie temperature. The dielectric constants of the planes perpendicular to the a- and c-axes of $Sr_2Nb_2O_7$ are stable near room temperature and have Curie temperatures around 1000 °C. The dielectric constants for the planes perpendicular to the b-axis are stable near room temperature; the dielectric constant for the plane perpendicular to the b-axis direction is lower than that for the other planes near room temperature, although the Curie temperature is low; and the dielectric constant increases sharply near 0 °C. In contrast, the Curie temperature of the plane perpendicular to the c-axes of $Sr_2Ta_2O_7$ is near −100 °C, and the dielectric constant of the planes perpendicular to the c-axes is higher than other planes, exceeding 200 at room temperature. Their results suggest that the dielectric constant of c-axes and the Curie temperature have a significant effect on the dielectric constant from room temperature to 300 °C. In the present study, the $Sr_2Ta_2O_7$–$Sr_2Nb_2O_7$ solid-solution system showed (110) and (200) planes in all compositions, except for the plane perpendicular to the c-axes. In contrast to them, the $Sr_2Ta_2O_7$–$La_2Ti_2O_7$ system showed the compositional dependence of orientation changes, and the substitution of the A-site with an element of smaller ionic radius should increase the Curie temperature. The compositional region with (010) orientation shows the lowest dielectric constant, which is consistent with the tendency in the single crystal noted by Nanamatsu et al.[19] Figure 7 also shows that the (010) plane-oriented thin film as confirmed by the 080 reflection in Figure 5 has the lowest dielectric constant. For the other orientations such as the compositional region with (041) orientation, the dielectric constant tends to increase as the influence of the c-axis becomes stronger. From the above, the orientation that eliminates the influence of the b-axis and the crystallinity that improves the orientation affect the improvement of the dielectric constant. Furthermore, since the a-axis has the same dielectric properties as the c-axis,[19] the dielectric constant is considered to be maximum in the (111) orientation, where the influence of the b-axis is smaller.

To improve the dielectric constant, the substrate temperature was reconsidered. The surface profile for the (111)-oriented region that showed the largest dielectric constant in the $0.35\mathrm{Sr_2Ta_2O_7}$–$0.65\mathrm{La_2Ti_2O_7}$ solid-solution films exhibited a porous structure [Figure 8a], which may reduce the effective dielectric constant. To improve the grain density, we considered that the porous structure could be reduced by lowering the substrate temperature. The film was formed by lowering the substrate temperature to 400 °C, which we expected to be sufficiently high to maintain the crystallinity of the $Sr_2Ta_2O_7$ composition side (Table 2). As a result, improvements in the grain density and crystallographic orientation were observed for the x = 0.35 composition [Figure 8b]. The dielectric constant of this sample was improved by ∼100%, and the temperature dependence of the dielectric constant, which was greater than 100, showed a good change of 7.1% in the range from room temperature to 300 °C (Figure 9).

https://doi.org/10.1021/acsomega.4c00788
ACS Omega 2024, 9, 25968−25975

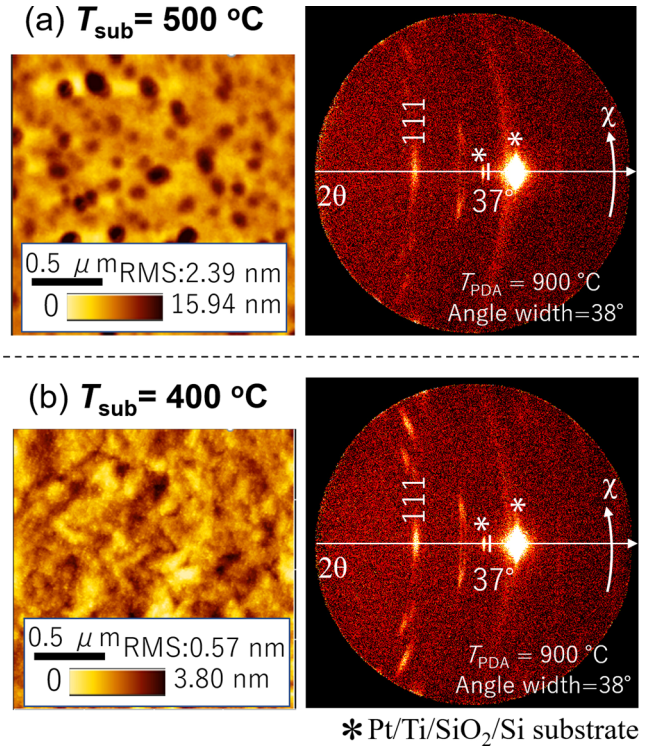

Figure 8. AFM images (left) and 2D-XRD images (right) of $0.35Sr_2Ta_2O_7$–$0.65La_2Ti_2O_7$ solid-solution films deposited at 500 and 400 °C and annealed at 900 °C.

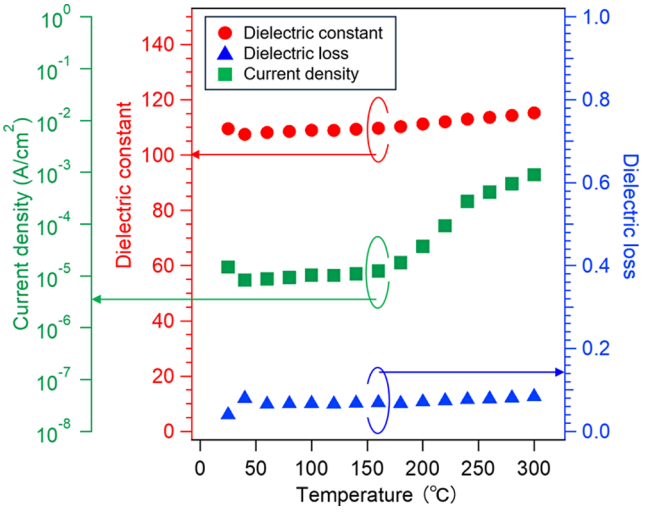

Figure 9. Temperature dependence of the dielectric constant (circles), dielectric loss (triangles), and current density (squares) for $0.35Sr_2Ta_2O_7$–$0.65La_2Ti_2O_7$ films deposited at 400 °C and annealed at 900 °C.

4. CONCLUSIONS

Thin films of $Sr_2Ta_2O_7$, $Sr_2Nb_2O_7$, $La_2Zr_2O_7$, and $La_2Ti_2O_7$ were grown by RF sputtering, and their physical properties were investigated. The crystallized $Sr_2Ta_2O_7$ and $La_2Zr_2O_7$ films exhibited highly oriented crystal structures. All of the films exhibited a small-grained structure. Compared to the La-containing films, the Sr-containing films showed larger-grained structures with few-hundred-nanometer grains. All of the films exhibited a dielectric constant of ∼40 at 1 MHz, which is similar to previously reported values of bulk crystals.[14,15] With respect to temperature stability, the Sr-containing films were more stable than the La-containing films. In particular, the crystallized $Sr_2Ta_2O_3$ film exhibited a $\Delta C/C$ of 4.9% with a dielectric constant of ∼50 in the temperature range from room temperature to 300 °C.

The results of A- and B-site substitution in the compositionally graded $xSr_2Ta_2O_7$–$(1-x)La_2Ti_2O_7$ samples showed that the $Sr_2Ta_2O_7$ structure was predominant over a wide compositional range and that the orientation of the thin film changed. The samples also showed a change in dielectric constant corresponding to the orientation, with the maximum dielectric constant occurring in the ⟨111⟩ direction, which has not been reported for single crystals. In addition, an increase in the thin film density led to an improvement of the dielectric properties. The crystallized $0.35Sr_2Ta_2O_7$–$0.65La_2Ti_2O_7$ film exhibited a $\Delta C/C$ value of 7.1% with a dielectric constant of 100 from room temperature to 300 °C.

These results suggest that the Sr-containing $A_2B_2O_7$ ferroelectric thin films exhibit strong potential for use in high-temperature operational film capacitor applications.

■ ASSOCIATED CONTENT

Data Availability Statement

The data used are available throughout the manuscript text and will be uploaded to the repository of the author's institute after publication.

Supporting Information

The Supporting Information is available free of charge at https://pubs.acs.org/doi/10.1021/acsomega.4c00788.

Sample structure and XRF analysis of compositionally graded solid-solution film (Figure S1); C–V properties of $Sr_2Ta_2O_7$ and $Sr_2Nb_2O_7$ films (Figure S2); peak shift behavior of the (110) reflection of $xSr_2Ta_2O_7$–$(1-x)Sr_2Nb_2O_7$ solid-solution films (Figure S3); current density properties of $xSr_2Ta_2O_7$–$(1-x)Sr_2Nb_2O_7$ solid-solution films (Figure S4); and XRD results of $xLa_2Zr_2O_7$–$(1-x)La_2Ti_2O_7$ solid-solution system (Figure S5) (PDF)

■ AUTHOR INFORMATION

Corresponding Author

Takahiro Nagata – *Research Center for Electronic and Optical Materials, National Institute for Materials Science (NIMS), Tsukuba 305-0044, Japan;* orcid.org/0000-0002-8591-2943; Email: NAGATA.Takahiro@nims.go.jp

Authors

Toyohiro Chikyow – *Center for Basic Research on Materials, NIMS, Tsukuba 305-0044, Japan*

Akira Ando – *Murata Manufacturing Co., Ltd., Nagaokakyo-shi, Kyoto 617-8555, Japan;* Present Address: Osaka Metropolitan University, Osaka 530-0001, Japan

Complete contact information is available at: https://pubs.acs.org/10.1021/acsomega.4c00788

Notes

The authors declare no competing financial interest.

■ ACKNOWLEDGMENTS

The authors are deeply grateful to Ms. Mika Watanabe and Mr. Kazuaki Nakane for technical assistance with physical property measurements and film growth. This work was supported by

"Advanced Research Infrastructure for Materials and Nanotechnology in Japan (ARIM)" of the Ministry of Education, Culture, Sports, Science and Technology (MEXT). Proposal Number JPMXP1223NM5168.

REFERENCES

(1) Morkoç, H.; Strite, S.; Gao, G. B.; Lin, M. E.; Sverdlov, B.; Burns, M. Large-band-gap SiC, III-V nitride, and II-VI ZnSe-based semiconductor device technologies. *J. Appl. Phys.* **1994**, *76*, 1363−1398, DOI: 10.1063/1.358463.

(2) Matsunami, H. Current SiC technology for power electronic devices beyond Si. *Microelectron. Eng.* **2006**, *83*, 2−4, DOI: 10.1016/j.mee.2005.10.012.

(3) Kachi, T. Recent progress of GaN power devices for automotive applications. *Jpn. J. Appl. Phys.* **2014**, *53*, No. 100210.

(4) Umezawa, H.; Nagase, M.; Kato, Y.; Shikata, S. High temperature application of diamond power device. *Diamond Relat. Mater.* **2012**, *24*, 201−205, DOI: 10.1016/j.diamond.2012.01.011.

(5) Neudeck, P. G.; Spry, D. J.; Chen, L. Y.; Beheim, G. M.; Okojie, R. S.; Chang, C. W.; Meredith, R. D.; Ferrier, T. L.; Evans, L. J.; Krasowski, M. J.; Prokop, N. F. Stable Electrical Operation of 6H−SiC JFETs and ICs for Thousands of Hours at 500 °C. *IEEE Electron Device Lett.* **2008**, *29*, 456−459, DOI: 10.1109/LED.2008.919787.

(6) Ikeda, K.; Umezawa, H.; Ramanujam, K.; Shikata, S. Thermally Stable Schottky Barrier Diode by Ru/Diamond. *Appl. Phys. Express* **2009**, *2*, No. 011202.

(7) Buttay, C.; Planson, D.; Allard, B.; Bergogne, D.; Bevilacqua, P.; Joubert, C.; Lazar, M.; Martin, C.; Morel, H.; Tournier, D.; Raynaud, C. State of the art of high temperature power electronics. *Mater. Sci. Eng.: B* **2011**, *176*, 283−288, DOI: 10.1016/j.mseb.2010.10.003.

(8) Szwagierczak, D.; Kulawik, J. Thick film capacitors with relaxor dielectrics. *J. Eur. Ceram. Soc.* **2004**, *24*, 1979−1985, DOI: 10.1016/S0955-2219(03)00358-3.

(9) Zang, J.; Jo, W.; Zhang, H.; Rödel, J. $Bi_{1/2}Na_{1/2}TiO_3$−$BaTiO_3$ based thick-film capacitors for high-temperature applications. *J. Eur. Ceram. Soc.* **2014**, *34*, 37−43, DOI: 10.1016/j.jeurceram-soc.2013.07.020.

(10) Shvartsman, V. V.; Lupascu, D. C. Lead-Free Relaxor Ferroelectrics. *J. Am. Ceram. Soc.* **2012**, *95*, 1−26, DOI: 10.1111/j.1551-2916.2011.04952.x.

(11) Kumaragurubaran, S.; Nagata, T.; Takahashi, K.; Ri, S.-G.; Tsunekawa, Y.; Suzuki, S.; Chikyow, T. $BaTiO_3$ based relaxor ferroelectric epitaxial thin-films for high-temperature operational capacitors. *Jpn. J. Appl. Phys.* **2015**, *54*, No. 04DH02.

(12) Kumaragurubaran, S.; Nagata, T.; Tsunekawa, Y.; Takahashi, K.; Ri, S.-G.; Suzuki, S.; Chikyow, T. Epitaxial growth of high dielectric constant lead-free relaxor ferroelectric for high-temperature operational film capacitor. *Thin Solid Films* **2015**, *592*, 29−33, DOI: 10.1016/j.tsf.2015.09.012.

(13) Kumaragurubaran, S.; Nagata, T.; Takahashi, K.; Ri, S.-G.; Tsunekawa, Y.; Suzuki, S.; Chikyow, T. Combinatorial synthesis of $BaTiO_3$−$Bi(Mg_{2/3}Nb_{1/3})O_3$ thin-films for high-temperature capacitors. *Jpn. J. Appl. Phys.* **2015**, *54*, No. 06FJ02.

(14) Zeb, A.; Milne, S. J. High temperature dielectric ceramics: a review of temperature-stable high-permittivity perovskites. *J. Mater. Sci.: Mater. Electron.* **2015**, *26*, 9243−9255, DOI: 10.1007/s10854-015-3707-7.

(15) Dittmer, R.; Anton, E. M.; Jo, W.; Simons, H.; Daniels, J. E.; Hoffman, M.; Pokorny, J.; Reaney, I. M.; Rödel, J. A High-Temperature-Capacitor Dielectric Based on $K_{0.5}Na_{0.5}NbO_3$-Modified $Bi_{1/2}Na_{1/2}TiO_3$−$Bi_{1/2}K_{1/2}TiO_3$. *J. Am. Ceram. Soc.* **2012**, *95*, 3519−3524, DOI: 10.1111/j.1551-2916.2012.05321.x.

(16) Kudo, A.; Kato, H.; Nakagawa, S. Water Splitting into H_2 and O_2 on New $Sr_2M_2O_7$ (M = Nb and Ta) Photocatalysts with Layered Perovskite Structures: Factors Affecting the Photocatalytic Activity. *J. Phys. Chem. B* **2000**, *104*, 571−575, DOI: 10.1021/jp9919056.

(17) Bouri, M.; Niederhauser, N.; Künzli, B.; Amsler, M.; Aschauer, U. Oxygen Evolution Reaction Activity of $Sr_2Ta_2O_7$ and $Sr_2Nb_2O_7$ Surfaces. *J. Phys. Chem. C* **2022**, *126*, 6556−6563, DOI: 10.1021/acs.jpcc.2c00649.

(18) Nanamatsu, S.; Kimura, M.; Doi, K.; Takahashi, M. Ferroelectric Properties of $Sr_2Nb_2O_7$ Single Crystal. *J. Phys. Soc. Jpn.* **1971**, *30*, 300−301, DOI: 10.1143/JPSJ.30.300.

(19) Nanamatsu, S.; Kimura, M.; Kawamura, T. Crystallographic and Dielectric Properties of Ferroelectric $A_2B_2O_7$ (A = Sr, B = Ta, Nb) Crystals and Their Solid Solutions. *J. Phys. Soc. Jpn.* **1975**, *38*, 817−824, DOI: 10.1143/JPSJ.38.817.

(20) Yamamoto, N.; Yagi, K.; Honjo, G.; Kimura, M.; Kawamura, T. New Phases of $Sr_2Ta_2O_7$ and $Sr_2Nb_2O_7$ Found by Electron Microscopy and Diffraction. *J. Phys. Soc. Jpn.* **1980**, *48*, 185−191, DOI: 10.1143/JPSJ.48.185.

(21) Koinuma, H.; Takeuchi, I. Combinatorial solid-state chemistry of inorganic materials. *Nat. Mater.* **2004**, *3*, 429−438, DOI: 10.1038/nmat1157.

(22) Ahmet, P.; Nagata, T.; Kukuruznyak, D.; Yagyu, S.; Wakayama, Y.; Yoshitake, M.; Chikyow, T. Composition spread metal thin film fabrication technique based on ion beam sputter deposition. *Appl. Surf. Sci.* **2006**, *252*, 2472−2476, DOI: 10.1016/j.apsusc.2005.05.078.

(23) Kido, H.; Komarneni, S.; Roy, S. Preparation of $La_2Zr_2O_7$ by Sol—Gel Route. *J. Am. Ceram. Soc.* **1991**, *74*, 422−424, DOI: 10.1111/j.1151-2916.1991.tb06899.x.

(24) Nanamatsu, S.; Kimura, M.; Doi, K.; Matsushita, S.; Yamada, N. A new ferroelectric: $La_2Ti_2O_7$. *Ferroelectrics* **1974**, *8*, 511−513, DOI: 10.1080/00150197408234143.

(25) JCPDS Powder Diffraction File-2 (PDF-2), 00−027−1402. 2004.

(26) Okuwada, K.; Nakamura, S.; Nozawa, H. Crystal growth of layered perovskite $Sr_2Nb_2O_7$ and $Sr_2Ta_2O_7$ film by the sol-gel technique. *J. Mater. Res.* **1999**, *14*, 855−860, DOI: 10.1557/JMR.1999.0114.

(27) JCPDS Powder Diffraction File-2 (PDF-2), 00−030−1304. 2004.

(28) Lotgering, F. K. Topotactical reactions with ferrimagnetic oxides having hexagonal crystal structures—I. *J. Inorg. Nucl. Chem.* **1959**, *9*, 113−123, DOI: 10.1016/0022-1902(59)80070-1.

(29) JCPDS Powder Diffraction File-2 (PDF-2), 00−052−0321. 2004.

(30) Shoyama, M.; Tsukuki, A.; Kato, K.; Murayama, N. Dielectric properties of alkoxy-derived $Sr_2Nb_2O_7$ thin films crystallized via rapid thermal annealing. *Appl. Phys. Lett.* **1999**, *75*, 561−562, DOI: 10.1063/1.124422.

(31) JCPDS Powder Diffraction File-2 (PDF-2), 00−050−0837. 2004.

(32) Cheng, X.; Qi, Z.; Li, T.; Zhang, G.; Li, C.; Zhou, H.; Wang, Y.; Yin, M. Infrared phonon modes and dielectric properties of $La_2Zr_2O_7$: Comparing thin film to bulk material. *Phys. Status Solidi B* **2012**, *249*, 854−857, DOI: 10.1002/pssb.201147313.

(33) JCPDS Powder Diffraction File-2 (PDF-2), 00−028−0517. 2004.

(34) Shao, Z.; Saitzek, S.; Roussel, P.; Ferri, A.; Bruyer, É.; Sayede, A.; Rguiti, M.; Mentré, O.; Desfeux, R. Microstructure and Nanoscale Piezoelectric/Ferroelectric Properties in $La_2Ti_2O_7$ Thin Films Grown on (110)-Oriented Doped Nb:SrTiO3 Substrates. *Adv. Eng. Mater.* **2011**, *13*, 961−969, DOI: 10.1002/adem.201100105.

(35) JCPDS Powder Diffraction File-2 (PDF-2), 00−004−0802. 2004.

https://doi.org/10.1021/acsomega.4c00788
ACS Omega 2024, 9, 25968−25975